

# Ab initio investigation of O<sub>2</sub> adsorption on Ca-doped LaMnO<sub>3</sub> cathodes in solid oxide fuel cells

Albert Aniagyei,<sup>a</sup> Nelson Y. Dzade,<sup>\*bc</sup> Richard Tia,<sup>a</sup> Evans Adei,<sup>a</sup> C. R. A. Catlow<sup>c</sup> and Nora H. de Leeuw<sup>bc</sup>

We present a Hubbard-corrected density functional theory (DFT+U) study of the adsorption and reduction reactions of oxygen on the pure and 25% Ca-doped LaMnO<sub>3</sub> (LCM25) {100} and {110} surfaces. The effect of oxygen vacancies on the adsorption characteristics and energetics has also been investigated. Our results show that the O<sub>2</sub> adsorption/reduction process occurs through the formation of superoxide and peroxide intermediates, with the Mn sites found to be generally more active than the La sites. The LCM25{110} surface is found to be more efficient for O<sub>2</sub> reduction than the LCM25{100} surface due to its stronger adsorption of O<sub>2</sub>, with the superoxide and peroxide intermediates shown to be energetically more favorable at the Mn sites than at the Ca sites. Moreover, oxygen vacancy defect sites on both the {100} and {110} surfaces are shown to be more efficient for O<sub>2</sub> reduction, as reflected in the higher adsorption energies calculated on the defective surfaces compared to the perfect surfaces.

We show from Lowdin population analysis that the O<sub>2</sub> adsorption on the pure and 25% Ca-doped LaMnO<sub>3</sub> surfaces is characterized by charge transfer from the interacting surface species into the adsorbed oxygen p<sub>g</sub> orbital, which results in weakening of the O–O bonds and its subsequent reduction. The elongated O–O bonds were confirmed via vibrational frequency analysis.

## 1. Introduction

The urgent need for low-cost, clean, sustainable energy for the future has stimulated interest in the development of alternative energy sources.<sup>1</sup> Solid oxide fuel cells (SOFCs) have been considered as one of the potential future energy power generation sources because of their high-energy efficiency and good fuel flexibility.<sup>2</sup> The development of reliable, low-cost and efficient SOFCs is, however, one of the critical scientific challenges in fuel cell applications.<sup>3</sup> These requirements may be achieved by reducing the operating temperature, which, however, results in internal loss at low temperatures (o500 1C).<sup>4</sup>

Platinum (Pt) is widely used as a cathode electro-catalyst, owing to its high catalytic reactivity toward the oxygen reduction reaction (ORR).<sup>5</sup> However, the high cost of Pt is a major limitation for its application, and reducing the Pt content and improving the ORR rate at the cathode remains a challenge for the development of fuel cells.<sup>6</sup> Strontium-doped lanthanum manganite (La<sub>1-x</sub>Sr<sub>x</sub>MnO<sub>3-d</sub>) is used as the cathode material

for commercial zirconia-based electrolyte SOFCs, owing to its stability, good electrical conductivity, efficient catalytic activity for the oxygen reduction reaction, and relatively low cost.<sup>7,8</sup> La<sub>1-x</sub>Sr<sub>x</sub>MnO<sub>3-d</sub> (x = 0.2–0.3) has also been actively used as a mixed ionic-electronic conducting (MIEC) cathode in SOFCs.<sup>9</sup>

Experimental studies<sup>10–12</sup> of the oxygen reduction reaction at the interface of a porous cathode/electrolyte or near triple-phase boundaries (TPBs), i.e. where the cathode, electrolyte, and oxygen species meet, propose that the ORR consists of many elementary steps involving the adsorption of oxygen as super-oxide (O<sub>2</sub><sup>-</sup>) or peroxide (O<sub>2</sub><sup>2-</sup>) species, dissociation of adsorbed O<sub>2</sub> to either O or O<sup>2-</sup>, and the incorporation of oxygen species into the bulk material.<sup>7,9,10</sup> Experimental techniques, such as impedance spectroscopy<sup>13</sup> and secondary ion mass spectrometry (SIMS), for probing the surface catalytic activity provide useful information about cathode performance. It is, however, extremely difficult to interpret the detailed information on elementary steps involved in the surface processes due to the complexity of the electrochemically active interfaces.<sup>14</sup>

In an experimental study<sup>15</sup> of the A-site doping of LaMnO<sub>3</sub>, carried out to establish the relative interfacial reactivity between the La<sub>1-x</sub>Sr<sub>x</sub>MnO<sub>3-d</sub> and yttria-stabilized zirconia (YSZ) for the dopants (A = Ca and Sr), it was reported that whilst a reaction was observed in the case of the Ca-doped LaMnO<sub>3</sub> sample forming CaZrO<sub>3</sub>, there was no reaction when a Sr dopant was used after long-term annealing at 1200 1C (up to 200 h).

<sup>a</sup>Department of Chemistry, Kwame Nkrumah University of Science and Technology, Kumasi, Ghana

<sup>b</sup>Department of Earth Sciences, Utrecht University, Princetonplein 8A, 3584 CB Utrecht, The Netherlands

<sup>c</sup>School of Chemistry, Cardiff University, Main Building, Park Place, CF10 3AT, Cardiff, UK. E-mail: DzadeNY@cardiff.ac.uk

The authors reported little difference in the performance of either material as a cathode for SOFC applications. The temperature at which the CaZrO<sub>3</sub> phase was formed is above the general operating temperatures of fuel cells and therefore does not present any fundamental problems.

The fundamental aspects of the reaction processes, including the geometries of the adsorbed superoxide or peroxide complexes, adsorption energies, and structural parameters remain unclear. Such information cannot be obtained directly from experimental work and the underlying physical driving forces that control reactivity of the oxygen species with LaMnO<sub>3</sub>-based surfaces are still poorly understood. However, with electronic structure calculations based on the density functional theory (DFT), it is possible to study computationally fundamental properties and processes that are largely inaccessible experimentally, including the interactions between crystal surfaces and adsorbates, as they are capable of accurately predicting

lowest-energy adsorption geometries and identifying charge transfer and other electronic effects.<sup>16–18</sup> For example, theoretical studies have predicted ionic transport through ABO<sub>3</sub>-type materials,<sup>19–23</sup> whereas Choi and co-workers have employed ab initio calculations to investigate the interactions between O<sub>2</sub> molecules and the MnO<sub>2</sub>-terminated (100) surfaces of (La,Sr)MnO<sub>3</sub> cathode materials.<sup>22,23</sup> Chen et al. have employed spin-polarized density functional theory and molecular dynamics (MD) calculations to study the kinetic behaviour of the oxygen reduction reaction and diffusion mechanisms on 25% Sr-doped LaMnO<sub>3</sub> (LSM).<sup>24</sup> They showed from their results that the O<sub>2</sub> adsorption/reduction process through the superoxide and peroxide intermediates is energetically more favorable at the Mn sites than at the Sr sites. In addition, higher adsorption energies were reported for O<sub>2</sub> adsorbed at the Mn sites on the (110) surface than on the (100) surface, which suggests that the former is more efficient for O<sub>2</sub> reduction than the latter. Oxygen vacancies were shown to enhance O<sub>2</sub> reduction kinetics, whereas O-ion migration through the bulk was found to be dominant over O-ion migration on the surface of the LSM cathode. Surprisingly, to date no systematic theoretical study has been conducted on the chemical activity of Ca-doped LaMnO<sub>3</sub>-based cathode materials towards oxygen reduction reactions, which makes this investigation timely.

In the present study, we have employed Hubbard-corrected DFT calculations to study the electronic and magnetic properties of pure and Ca-doped LaMnO<sub>3</sub> {100} and {110} surfaces, before subsequently unravelling the energetics of the oxygen adsorption and reduction at the surfaces. The {100} and {110} surfaces were considered for the O<sub>2</sub> reduction reactions, because they are the most stable surfaces of LaMnO<sub>3</sub> according to surface-stability calculations.<sup>25</sup> Furthermore, it has been reported that ionic diffusion occurs along the {110} direction.<sup>26</sup> The LaMnO<sub>3</sub>{100} surface can be LaO- or MnO-terminated, but we have considered only the MnO-terminated surface for the O<sub>2</sub> adsorption calculations, because in ABO<sub>3</sub> cathode materials the B cation sites are known to be more active than A cation sites toward oxygen reduction.<sup>27</sup> For the {110} surface, the LaMnO-termination was considered for the O<sub>2</sub> adsorption calculations

which permits the examination of the oxygen reduction at both La and Mn cation sites. For all the stable O<sub>2</sub> adsorption configurations, the vibrational frequencies and the Löwdin population analyses of the adsorbed surface oxygen species are also reported and discussed.

## 2. Computational details

The calculations were carried out within the Kohn–Sham DFT formalism,<sup>28</sup> using a plane-wave basis set as implemented in the Quantum-ESPRESSO code.<sup>29</sup> The Perdew–Burke–Ernzerhof (PBE) generalized gradient approximation (GGA) was employed for the exchange and correlation terms.<sup>30</sup> The plane-wave basis set cut-offs for the smooth part of the wave function and the augmented density were set to 40 and 420 Ry, respectively, which ensured convergence of the total energy to within 0.01 eV Å<sup>-1</sup>. The Brillouin zone for the bulk LaMnO<sub>3</sub> was sampled using a 4 × 4 × 4 Monkhorst–Pack k-points mesh.<sup>31</sup> We have investigated the symmetric Pm3m cubic structure (Fig. 1), because it is stable under SOFC operating conditions (above 500 °C in ambient air).<sup>32,33</sup> All calculations were spin-polarized in order to describe accurately the magnetic properties of the pure, Ca-doped LaMnO<sub>3</sub> structure, and the triplet ground state of oxygen. The DFT+U approach<sup>34</sup> with a U<sub>eff</sub> value of 4.0 eV for Mn ions was employed to correct the large self-interaction error inherent in standard DFT-GGA methods for mid-to-late first-row transition metal oxides.<sup>35,36</sup> The effect of the implementation of DFT+U on LaMnO<sub>3</sub> was checked by calculating the projected density of states (PDOS) of the bulk LaMnO<sub>3</sub> system with and without DFT+U correction, as shown in Fig. 2. The PDOS of LaMnO<sub>3</sub> shows a half-metallic ferromagnetic structure with a band gap between the valence band maximum (VBM) and conduction band minimum (CBM) calculated at 2.66 eV with standard DFT and 3.66 eV with DFT+U. This behaviour is

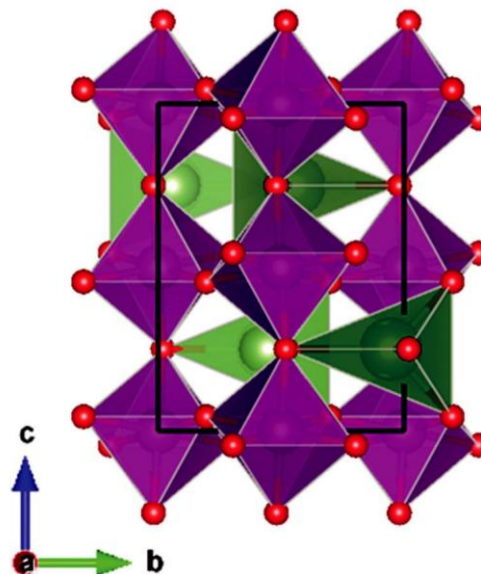


Fig. 1 Structure of LaMnO<sub>3</sub> in terms of MnO<sub>6</sub> and LaO<sub>4</sub> octahedra.

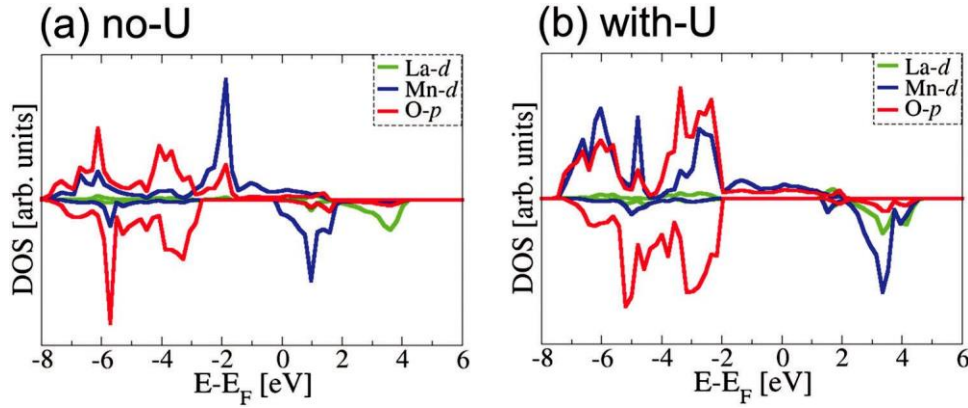


Fig. 2 Projected density of states of (PDOS) of LaMnO<sub>3</sub> without (a) and with (b) Hubbard U correction.

consistent with the prediction from previous studies.<sup>37–39</sup> We have considered different possible magnetic orderings at the Mn<sup>3+</sup> site in the 25% Ca-doped LaMnO<sub>3</sub> structure and found that the ferromagnetic (FM) ordering is 0.3 eV more stable than the antiferromagnetic (AFM) ordering. The predicted lattice constant of the defect-free Ca-doped La<sub>0.75</sub>Ca<sub>0.25</sub>MnO<sub>3</sub> is slightly reduced (3.865 Å) compared to pure LaMnO<sub>3</sub> (3.869 Å), which is in agreement with the experimental observation that the lattice constant decreases with increasing dopant content.<sup>40</sup> We observe further reduction in the lattice parameter of the oxygen deficient Ca-doped LaMnO<sub>3</sub> containing surface oxygen vacancy (3.793–3.806 Å).

The {100} and {110} surface structures were created from the fully optimized bulk structure using the METADISE code,<sup>41</sup> which ensures the creation of surfaces with zero dipole moment perpendicular to the surface plane, as is required for reliable and realistic surface calculations.<sup>42</sup> The fully relaxed bulk structures were used to create the surfaces in order to eliminate the presence of fictitious forces during surface relaxation. The surfaces were modelled using a slab model comprising of eight atomic layers with a vacuum size of 12 Å introduced in the z-direction, which is large enough to avoid any spurious interaction between periodic slab images. Similar to previous studies,<sup>14</sup> all surface calculations for the interactions between molecular oxygen species and La<sub>0.75</sub>Ca<sub>0.25</sub>MnO<sub>3</sub> surfaces were performed by relaxing the top three layers while keeping the bottom five layers fixed at the bulk parameters.

The adsorption energy was calculated according to the following relation:

$$E_{\text{ads}} = E_{\text{surface+O}_2} - (E_{\text{surface}} + E_{\text{O}_2}) \quad (1)$$

where  $E_{\text{surface+O}_2}$  is the total energy of the substrate–adsorbate system in the equilibrium state, and  $E_{\text{surface}}$  and  $E_{\text{O}_2}$  are the total energies of the substrate (clean surface) and adsorbate (free O<sub>2</sub> molecule in the spin triplet state), respectively. The O<sub>2</sub> bond length  $d(\text{O}–\text{O})$  and stretching vibrational frequency  $\nu(\text{O}–\text{O})$  were calculated at 1.235 Å and 1558 cm<sup>-1</sup>, respectively,

both of which are in good agreement with experimental results (1.207 Å and 1550 cm<sup>-1</sup>)<sup>43,44</sup> as well as with other DFT

calculations between the O<sub>2</sub> molecule and the interacting surface species were analyzed with the Loewdin population scheme.

### 3. Results and discussions

#### 3.1 Characterization of Ca-doped LaMnO<sub>3</sub> surfaces

Experimentally, the defective surface structures of La<sub>1-x</sub>A<sub>x</sub>MnO<sub>3</sub> are known to be dependent on partial pressure of oxygen and temperature.<sup>47</sup> Hence, a simplified surface model of La<sub>0.75</sub>Ca<sub>0.25</sub>MnO<sub>2.75</sub> (LCM25) was constructed by substituting a La<sup>3+</sup> ion by Ca<sup>2+</sup> in the {110} and {100} LaMnO<sub>3</sub> surfaces, which leads to four possible models, as shown in Fig. 3. Both {110} and {100} supercells of 25% Ca-doped LaMnO<sub>3</sub> contain a total of 20 ions (3 La, 1 Ca, 4 Mn, and 12 O ions). Additionally, we have calculated the formation energy of an oxygen vacancy located in the top layer, based on the reaction of La<sub>0.75</sub>Ca<sub>0.25</sub>MnO<sub>3</sub> surface - La<sub>0.75</sub>Ca<sub>0.25</sub>MnO<sub>3-x</sub> + 1/2O<sub>2</sub>(g) using the relation:

$$DE_f = E(\text{defective}) + 1/2E(\text{O}_2) - E(\text{perfect}) \quad (2)$$

where  $E[\text{defective}]$ ,  $E[\text{perfect}]$  and  $E[\text{O}_2]$  are the total energies of defective surface, the perfect Ca-doped LaMnO<sub>3</sub> surface and the triplet oxygen molecule, respectively. Summarized in Table 1 are the calculated energies for oxygen-vacancy formation at the CaMnO-terminated {110} and the MnO<sub>2</sub>-terminated {100} LCM25 surfaces. Relatively low vacancy formation energies were computed for the doped surfaces compared to the pure surfaces,

which indicated that Ca doping may facilitate the oxygen-vacancy formation in LaMnO<sub>3</sub>. For the pure LaMnO<sub>3</sub> surface model, an oxygen deficient surface was generated by removing an oxygen anion (O<sup>2-</sup>), from the top layer.

With respect to the Ca-doped LaMnO<sub>3</sub>{110} and {100} surfaces, models L1 with the Ca ion in/near the topmost layers (Fig. 3a and b) were found to possess the lowest oxygen-vacancy formation energies and they are therefore the surfaces used for the oxygen adsorption calculations. The O-vacancy formation energies calculated in the present study for the Ca-doped LaMnO<sub>3</sub> surfaces are similar to those reported for Sr-doped

LaMnO<sub>3</sub> surfaces.<sup>24</sup> Shown in Fig. 4 are the top and side views of the Ca-doped LaMnO<sub>3</sub>{110} and {100} surface models, showing

results.<sup>45,46</sup> The nature of the bonding and charge

transfer the different adsorption sites explored for O<sub>2</sub> adsorption.

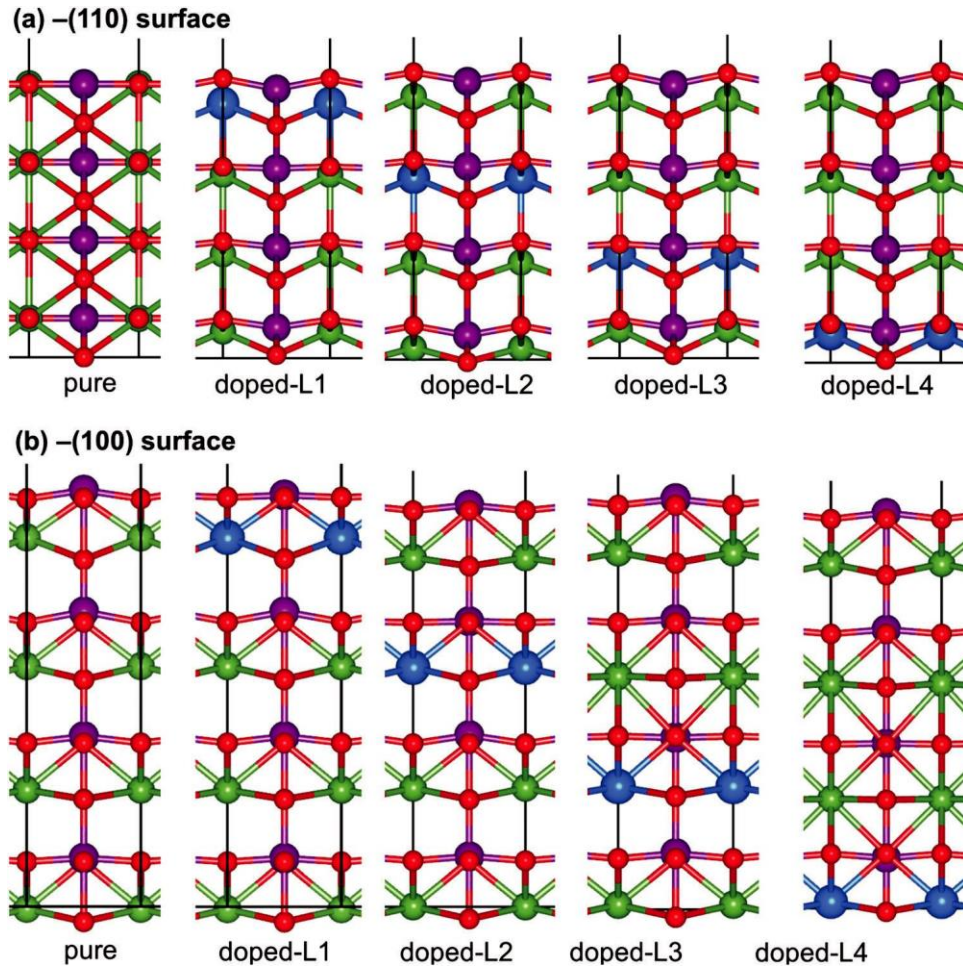


Fig. 3 Pure and Ca-doped  $\text{LaMnO}_3$  surface models; (a) L1 is  $\text{CaMnO}$ -terminated and L2–L4 are  $\text{LaMnO}$ -terminated (110) surface structures, (b)  $\text{MnO}_2$ -terminated (100) LCM25 surface structures. Colour code: green = La, blue = Ca, purple = Mn, and red = O.

Table 1 Calculated oxygen vacancy formation energies (in eV) with (bracket) and without Hubbard U correction at the (1 1)  $\text{CaMnO}$ -terminated (110) and  $\text{MnO}_2$ -terminated (100) LCM25 surfaces models in Fig. 2

Surface model	{110}	{100}
L1	4.23 (3.52)	3.25 (1.83)
L2	4.45 (3.87)	3.68 (2.30)
L3	4.53 (3.73)	3.97 (2.71)
L4	4.54 (3.86)	4.12 (2.98)
$\text{LaMnO}_3$	4.56 (4.23)	4.31 (3.61)

### 3.2 $\text{O}_2$ adsorption on the undoped perfect and oxygen-deficient $\text{LaMnO}_3\{110\}$ surfaces

We have considered both molecular and dissociative adsorption of  $\text{O}_2$  on the selected (1 1) and (2 1) surface models at 0.5 ML and 0.25 ML coverages, respectively, where a monolayer (ML) is defined as one oxygen molecule per surface cation. For the adsorption of molecular oxygen on the pure  $\text{LaMnO}_3$  surfaces, we have considered two initial adsorption modes; the end-on type, where  $\text{O}_2$  vertically binds to the surface atom, and a side-on type, where  $\text{O}_2$  binds parallel to the surface atom. In all calculations, the surface and adsorbate atoms were free to move

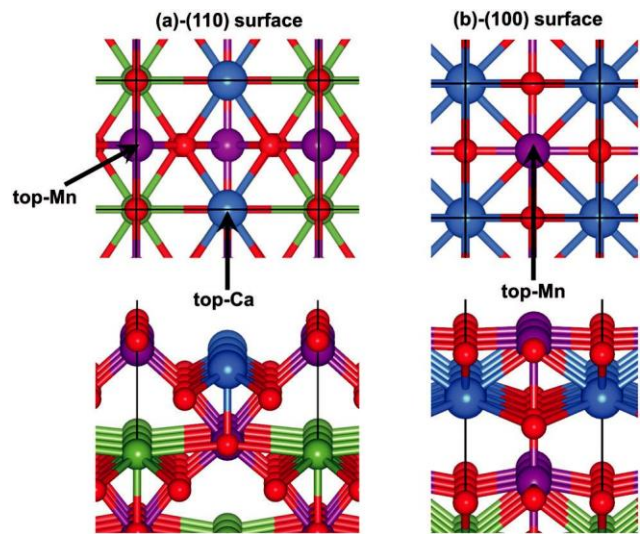


Fig. 4 Schematic representation of the side and top views of the (1 1) slab model of (a) LCM25{110} and (b) LCM25{100} supercells showing the different adsorption sites explored. Colour code: green = La, blue = Ca, purple = Mn, and red = O.

Table 2 Calculated adsorption energy ( $E_{\text{ads}}$ ), charge ( $q$ ), relevant bond distances ( $d$ ) of molecular ( $\text{O}_2$ ) oxygen on perfect and defective  $\{110\}$  surface of pure  $\text{LaMnO}_3$ ; O–O stretching vibrational frequency ( $\nu$ ) of the adsorbed  $\text{O}_2$ ; and calculated gas phase  $d(\text{O}–\text{O}) = 1.229 \text{ \AA}$  and the  $\nu(\text{O}–\text{O}) = 1558 \text{ cm}^{-1}$

	Config	$E_{\text{ads}}$	$ q $	$d(\text{O}–\text{Mn})^{\text{a}}$	$d(\text{O}–\text{La})^{\text{b}}$	$d(\text{O}–\text{O})$	$\nu(\text{O}–\text{O})$
		(eV)	(e)	( $\text{\AA}$ )	( $\text{\AA}$ )	( $\text{\AA}$ )	( $\text{cm}^{-1}$ )
Perfect	M1	0.96	0.04	1.832	—	1.313	1118
	M2	1.07	0.06	1.853	—	1.404	774
	M3	0.79	0.06	—	2.200	1.323	705
	M4	1.60	0.06	—	2.275	1.408	759
	M5	3.58	0.06	1.987	2.327	1.491	511
	D1	1.63	0.10	1.597	1.764	—	—
Defective	M1	1.34	0.04	1.834	—	1.353	949
	M2	2.32	0.06	1.844	—	1.445	636
	M3	1.14	0.04	—	2.174	1.315	1108
	M4	1.84	0.06	—	2.130	1.483	497
	M5	4.59	0.08	1.911	2.348	1.515	439
	M6	3.50	0.04	—	—	1.300	416
	D1	6.43	0.09	1.653	—	—	—
	D2	8.89	0.10	1.874	2.329	—	—

<sup>a</sup> The shortest distance between an adsorbed oxygen species and the Mn ions.

<sup>b</sup> The shortest distance between an adsorbed oxygen species and La ions.

during the geometry optimization to obtain the lowest energy structure after relaxation.

The calculated adsorption energies, atomic charges, optimized interatomic bond distances and vibrational frequencies are summarized in Table 2. Generally, we found the side-on configurations are energetically more favorable than the end-on configurations. The adsorption energy of the side-on  $\text{O}_2$  at the Mn site (Fig. 5, M2) is calculated at 1.07 eV compared to 0.96 eV for the end-on  $\text{O}_2$  at the Mn site (Fig. 5, M1). The O–Mn interatomic bond distances between the interacting oxygen atom (O) and the surface Mn cation for M1 and M2 are calculated at 1.83  $\text{\AA}$  and 1.85  $\text{\AA}$ , respectively. When adsorbed at the La cation site, the adsorption energies for the end-on and side-on configurations (Fig. 5, M3 and M4) of  $\text{O}_2$  are calculated at 0.79 eV and 1.60 eV, respectively. The O–La interatomic bond distances between the interacting oxygen atom (O) and the surface La cation site for M3 and M4 are calculated at 2.20  $\text{\AA}$  and 2.28  $\text{\AA}$ , respectively. The lowest-energy adsorption structure

is calculated for  $\text{O}_2$  adsorbed side-on at the La–Mn bridge site (Fig. 5, M5), with an adsorption energy of 3.58 eV. The interacting O–La and O–Mn interatomic distances are calculated at 2.33  $\text{\AA}$  and 1.99  $\text{\AA}$  respectively.

In all the molecularly adsorbed  $\text{O}_2$  structures, we observe elongation of the O–O bonds, which indicates that they are weakened. In M1 and M2, the O–O bond is calculated at 1.30  $\text{\AA}$  and 1.40  $\text{\AA}$ , respectively, compared to 1.24  $\text{\AA}$  for the gas phase  $\text{O}_2$  molecule. Similarly, for M3 and M4 adsorption configurations at the La site, the O–O bond is calculated at 1.32  $\text{\AA}$  and 1.41  $\text{\AA}$ , respectively. The largest O–O bond elongation (1.49  $\text{\AA}$ ) is observed in the M5 configuration, where the  $\text{O}_2$  molecules adsorb at the bridge La–Mn site. From Loewdin population analysis, we found that the adsorption of  $\text{O}_2$  is characterized by a small net charge transfer (0.04–0.10 e<sup>-</sup>) from the interacting topmost bound La and Mn cations, which is responsible for the elongation of the O–O bond lengths reported in Table 2. The elongated O–O bonds were confirmed through vibrational frequency analysis, where we found lower O–O stretching frequency for the adsorbed  $\text{O}_2$  compared to the gas phase molecule. The O–O stretching vibrational frequencies for  $\text{O}_2$  adsorbed end-on and side-on at the top Mn and La cation sites and bridge-LaMn sites are assigned to 1118, 774, 705, 759 and

511  $\text{cm}^{-1}$ , respectively, all of which are lower than in the gas phase molecule (1558  $\text{cm}^{-1}$ ). Based on the calculated stretching frequencies and the O–O bond lengths of the

adsorbed  $\text{O}_2$  (1.30–1.32  $\text{\AA}$ ) and (1.40–1.49  $\text{\AA}$ ), which are similar to that of the  $\text{O}_2^-$  ion (1.33  $\text{\AA}$ ) and  $\text{O}_2^{2-}$  (1.44),<sup>48,49</sup> we deduced that the adsorbed molecular oxygen species on the pure  $\text{LaMnO}_3\{110\}$  surfaces are superoxo ( $\text{O}_2^-$ ) and peroxo ( $\text{O}_2^{2-}$ ) species. The significant elongation of the O–O bond of the lowest-energy M5 structure suggests that this molecular adsorbed state is a likely precursor for  $\text{O}_2$  dissociation on the pure  $\text{LaMnO}_3\{110\}$ .

Compared to the M5 structure, the dissociative adsorption of  $\text{O}_2$  on the pure  $\text{LaMnO}_3\{110\}$  is found to be less exothermic ( $E_{\text{ads}} = 1.63 \text{ eV}$ ), which suggests that the  $\text{LaMnO}_3\{110\}$  favours molecular  $\text{O}_2$  adsorption rather than dissociative adsorption. The dissociated  $\text{O}^{2-}$  ions adsorb preferentially at top-La and Mn sites (Fig. 5, D2) and draw a combined charge of 0.10 e from the interacting surface La and Mn cation sites.

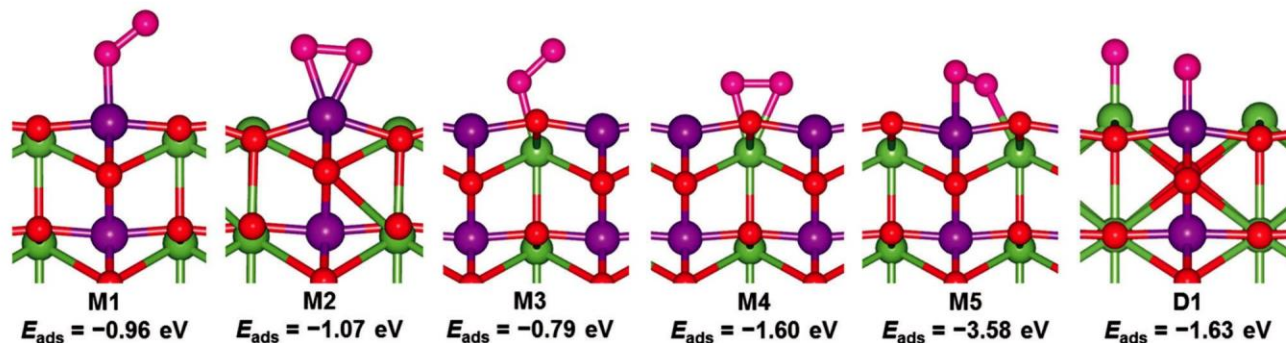


Fig. 5 Side views of the optimized geometry structures of oxygen molecule on  $(1\ 1)$  undoped perfect  $\text{LaMnO}_3\{110\}$ . Colour code: green = La, purple = Mn, and red = O.

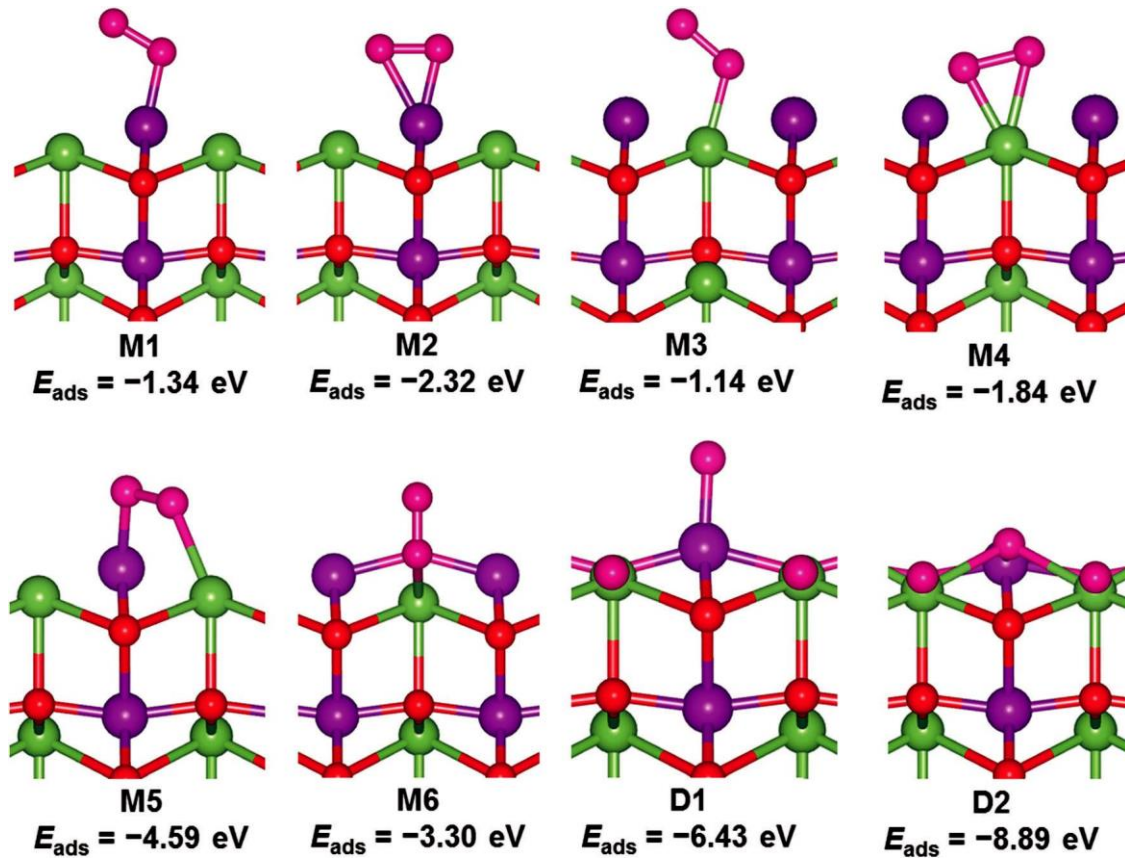


Fig. 6 Side views of the optimized geometry structures of oxygen molecule on (1 1) undoped defective  $\text{LaMnO}_3 \times \{110\}$ . Colour code: green = La, purple = Mn, and red = O.

Similar to the perfect  $\text{LaMnO}_3\{110\}$  surface, we have considered several adsorption geometries and sites at the defective  $\text{LaMnO}_3 \times \{110\}$  surface, containing an O-vacant site at the surface, in order to determine the lowest-energy adsorption structures. The optimized adsorption structures are shown in Fig. 6, whereas the calculated adsorption energies, atomic charges, optimized interatomic bond distances and vibrational frequencies are listed in Table 2. The adsorption energies for the end-on and side-on configurations of  $\text{O}_2$  bound at the top Mn cation sites (Fig. 6, M1 and M2) are calculated at 1.34 eV and 2.32 eV, respectively. The interatomic Mn–O; O–O bond distances for  $\text{O}_2$  bound end-on at the top-Mn sites are calculated to be 1.834 Å; 1.35 Å for M1 and 1.844 Å; 1.45 Å for M2. For the end-on and side-on configurations of  $\text{O}_2$  bound at the top La cation sites (Fig. 6, M3 and M4), the adsorption energies are calculated at 1.14 and 1.84 eV, respectively, with the interacting O–La interatomic bond distances for M3 and M4 calculated at 2.17 Å and 2.13 Å, respectively. As on the perfect  $\{110\}$  surface, the lowest-energy adsorption structure was obtained for  $\text{O}_2$  adsorbed side-on at the LaMn bridge site (Fig. 6, M5), releasing an adsorption energy of 4.59 eV. The interacting O–La and O–Mn interatomic distances are calculated at 2.348 Å and 1.911 Å, respectively. When  $\text{O}_2$  is adsorbed end-on at the O-vacant site, an adsorption energy of 3.50 eV is calculated, with the O–O interatomic bond slightly elongated (1.24 Å - 1.30 Å).

Similar to the perfect undoped  $\{110\}$  surface, we assigned superoxo ( $\text{O}_2^-$ ) and peroxo ( $\text{O}_2^{2-}$ ) species based on the calculated stretching frequencies and the O–O bond lengths of the adsorbed  $\text{O}_2$  (1.32 - 1.35 Å) and (1.45 - 1.48 Å), which are similar to that of the  $\text{O}_2^-$  ion (1.33 Å) and  $\text{O}_2^{2-}$  (1.44).<sup>48,49</sup> Compared to the perfect surface, the dissociative  $\text{O}_2$  adsorption structures (Fig. 6 D1 and D2) on the defective  $\text{LaMnO}_3 \times \{110\}$  are found to be energetically more favoured than molecular adsorption on the perfect  $\{110\}$  surface, although all adsorptions energies are highly exothermic. In the D1 structure, one of the dissociated  $\text{O}^{2-}$  ions is incorporated into the oxygen vacancy site, whereas the other one is adsorbed at a top Mn site, releasing an energy of 6.43 eV in the process. When both dissociated  $\text{O}^{2-}$  ions are incorporated at the vacancy site (D2), an even larger adsorption energy is released of 8.89 eV.

### 3.3 $\text{O}_2$ adsorption on the undoped perfect and oxygen-deficient $\text{LaMnO}_3\{100\}$ surfaces

Two stable adsorption configurations were obtained for the interaction of  $\text{O}_2$  with the perfect  $\text{LaMnO}_3\{100\}$ : end-on and side-on at a top Mn-site (Fig. 7, M1-perf and M2-perf). Listed in Table 3 are the calculated adsorption energies and relevant interatomic bond distances. The adsorption energies for  $\text{O}_2$  adsorbed end-on and side-on at a top Mn-site are calculated at 1.43 and 1.37 eV, respectively, indicating the small energetic

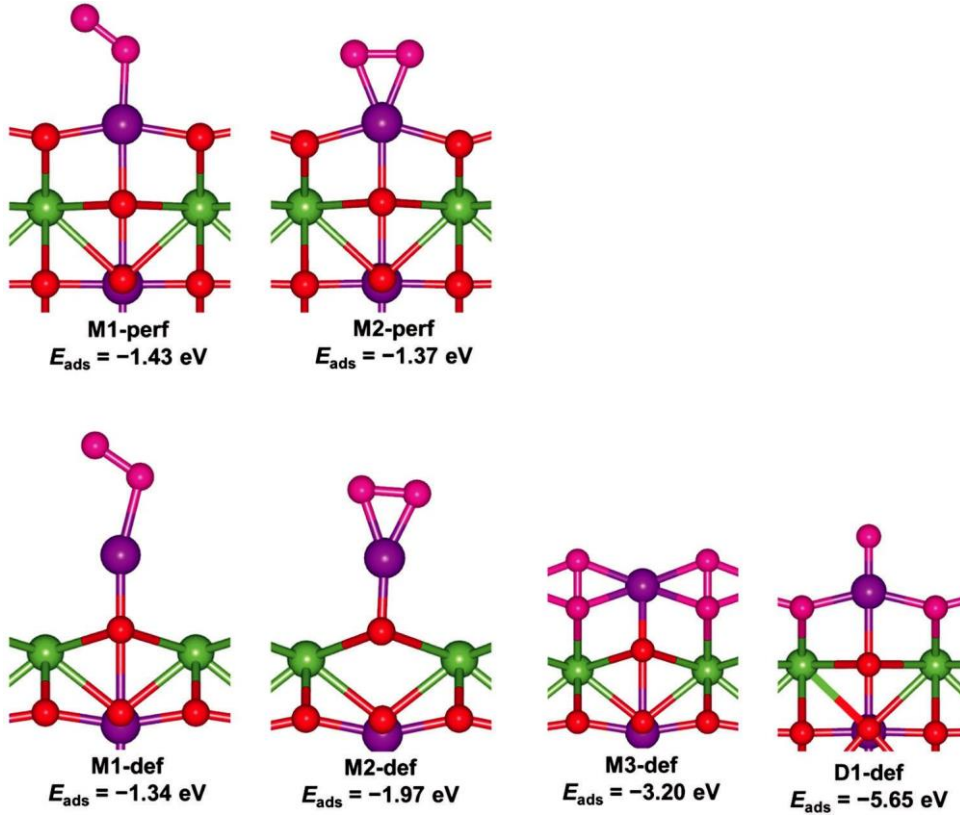


Fig. 7 Side views of the optimized geometry structures of oxygen molecule on (1 1) undoped perfect (top) and defective (down)  $\text{LaMnO}_3\{100\}$ . Colour code: green = La, purple = Mn, and red = O.

Table 3 Calculated adsorption energy ( $E_{\text{ads}}$ ), charge ( $q$ ), relevant bond distances ( $d$ ) of molecular ( $\text{O}_2$ ) oxygen on the on perfect and defective  $\{100\}$ - $(1\ 1)$  surface of pure  $\text{LaMnO}_3$ ; O–O stretching vibrational frequency ( $\nu$ ) of the adsorbed  $\text{O}_2$ ; and calculated gas phase  $d(\text{O}-\text{O}) = 1.229\ \text{\AA}$  and the  $\nu(\text{O}-\text{O}) = 1558\ \text{cm}^{-1}$

Surface	Config	$E_{\text{ads}}$ (eV)	$ q $ (e)	$d(\text{O}-\text{Mn})^a$ ( $\text{\AA}$ )	$d(\text{O}-\text{O})$ ( $\text{\AA}$ )	$\nu(\text{O}-\text{O})$ ( $\text{cm}^{-1}$ )
Perfect	M1	1.43	0.04	1.838	1.282	1271
	M2	1.37	0.02	1.853	1.364	919
Defective	M1	1.34	0.02	1.748	1.272	1320
	M2	1.97	0.06	1.810	1.391	820
	M3	3.20	0.08	—	1.529	421
	D1	5.65	0.10	1.590	—	—

<sup>a</sup> The shortest distance between an adsorbed oxygen species and a Mn ion.

preference for an end-on  $\text{O}_2$  configuration. The interatomic Mn–O and O–O bond distances for  $\text{O}_2$  bound end-on at top-Mn sites are calculated to be  $1.853\ \text{\AA}$  and  $1.28\ \text{\AA}$ , respectively. For the side-on top-Mn  $\text{O}_2$  configuration, the two interacting Mn–O distances are  $1.838$  and  $1.842\ \text{\AA}$ , with the O–O bond converged at  $1.36\ \text{\AA}$ , compared to  $1.24\ \text{\AA}$  for the gas phase  $\text{O}_2$  molecule.

On the defective  $\text{LaMnO}_3\{100\}$  surface, the side-on adsorption of  $\text{O}_2$  at the top-Mn site (Fig. 7, M2-def) is found to be bound more strongly by  $0.63\ \text{eV}$  than the end-on top-Mn site (Fig. 7, M1-def). Summarized in Table 4 are the calculated adsorption

energies and relevant interatomic bond distances. The adsorption of  $\text{O}_2$  by inserting it end-on into the oxygen vacancy site (Fig. 7, M3-def) released an adsorption energy of  $3.20\ \text{eV}$ .

Furthermore, the dissociative adsorption of  $\text{O}_2$  on the defective  $\text{LaMnO}_3\{100\}$  is found to be highly exothermic ( $E_{\text{ads}} = 5.65\ \text{eV}$ ), which suggests that the defective  $\text{LaMnO}_3\{100\}$  favours dissociative  $\text{O}_2$  adsorption rather than molecular adsorption, similar to the findings on the defective  $\text{LaMnO}_3\{110\}$  surface. The dissociated  $\text{O}^2$  ions at the defective  $\text{LaMnO}_3\{100\}$  adsorb preferentially at top-Mn sites and in the oxygen vacancy sites (Fig. 7, D1-def).

#### 3.4 $\text{O}_2$ adsorption on the perfect and oxygen-deficient $\text{LaMnO}_3\{110\}$ surfaces

3.4.1  $\text{O}_2$  adsorption on perfect  $\text{LaMnO}_3\{110\}$  surface. Shown in Fig. 8 are the optimized adsorption structures of  $\text{O}_2$  on the Ca-doped perfect  $\{110\}$  surface, whereas the calculated adsorption energies and the optimized interatomic bond distances are summarized in Table 4. The adsorption energies of the end-on and side-on configurations (Fig. 8, M1 and M2) of  $\text{O}_2$  adsorbed at the top Mn sites are  $0.84\ \text{eV}$  and  $0.72\ \text{eV}$ , respectively. The formation of M1 and M2 intermediates on the perfect  $\text{LaMnO}_3\{110\}$  surface is accompanied by the lengthening of the O–O bond, calculated at  $1.30\ \text{\AA}$  and  $1.41\ \text{\AA}$ , respectively, compared to the gas phase distance of  $1.24\ \text{\AA}$ . The interatomic O–Mn bond distances between the interacting oxygen atom and

Table 4 Calculated adsorption energy ( $E_{\text{ads}}$ ), charge ( $q$ ), relevant bond distances ( $d$ ) of molecular ( $\text{O}_2$ ) oxygen on perfect and defective  $\{110\}$ - $(1\ 1)$  surface of LCM25; O–O stretching vibrational frequency ( $\nu$ ) of the adsorbed  $\text{O}_2$ ; and calculated gas phase  $d(\text{O}=\text{O}) = 1.229\ \text{\AA}$  and the  $\nu(\text{O}=\text{O}) = 1558\ \text{cm}^{-1}$ . The  $\{110\}$ - $(2\ 1)$  values are given in parenthesis

Surface	Config	$E_{\text{ads}}$ (eV)	$ q $ (e)	$d(\text{O}-\text{Mn})^{\text{a}}$ ( $\text{\AA}$ )	$d(\text{O}-\text{Ca})^{\text{a}}$ ( $\text{\AA}$ )	$d(\text{O}-\text{O})$ ( $\text{\AA}$ )	$\nu(\text{O}=\text{O})$ ( $\text{cm}^{-1}$ )
Perfect	M1	0.84 ( 0.97)	0.26	1.850 (1.941)	—	1.303 (1.328)	1163
	M2	0.72 ( 1.22)	0.44	1.860 (1.816)	—	1.408 (1.453)	691
	M3	0.94 ( 1.26)	0.33	—	2.319 (2.283)	1.310 (1.348)	1138
	M4	2.40 ( 3.36)	0.53	1.874 (1.892)	2.268 (2.177)	1.422 (1.451)	710
	D1	+0.10 ( 3.70)	0.40	1.598 (1.622)	2.229 (2.113)	—	—
Defective	M1	1.30 ( 1.38)	0.44	1.902	(2.199)	1.406 (1.455)	1284
	M2	2.14 ( 3.67)	0.47	1.829 (1.944)	(2.272)	1.436 (1.525)	615
	M3	1.12 ( 3.37)	0.50	—	2.256	1.347 (1.510)	979
	M4	3.28	0.65	1.847	2.280	1.478	532
	M5	2.94	0.76	—	—	1.510	433
	D1	5.79 ( 5.77)	0.91	1.632 (1.654)	—	—	—
	D2	3.52 ( 3.82)	1.00	—	2.168 (2.103)	—	—
	D3	6.93 ( 7.50)	1.26	1.584 (1.778)	2.152 (2.296)	—	—

<sup>a</sup> The shortest distance between an adsorbed oxygen species and a Mn or Ca ion on  $\{110\}$  surface.

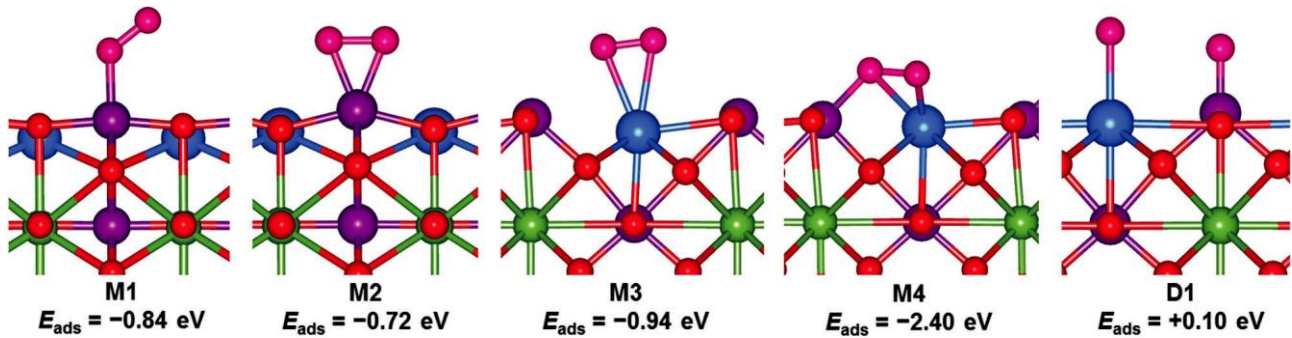


Fig. 8 Side views of the optimized geometry structures of oxygen molecule on perfect  $(1\ 1)$   $\text{La}_{0.75}\text{Ca}_{0.25}\text{MnO}_3\{110\}$ . Colour code: green = La, blue = Ca, purple = Mn, and red = O.

the surface Mn cation for M1 and M2 structures are calculated at  $1.85\ \text{\AA}$  and  $1.86\ \text{\AA}$ , respectively. No stable end-on configuration was obtained at the top-Ca site as it converts to a side-on configuration during geometry optimization (Fig. 8, M3), with an exothermic adsorption energy of  $0.94\ \text{eV}$ . The O–Ca inter-atomic distance is calculated at  $2.319\ \text{\AA}$  whereas the O–O bond length is obtained at  $1.31\ \text{\AA}$ . When adsorbed in a side-on configuration at bridge Ca–Mn sites (Fig. 8, M4), an adsorption energy of  $2.40\ \text{eV}$  was released, with the O–Ca and O–Mn interatomic distances calculated at  $2.268\ \text{\AA}$  and  $1.874\ \text{\AA}$ , respectively. The O–O bond is significantly elongated in the bridge Ca–Mn adsorption mode, calculated at  $1.42\ \text{\AA}$  compared to  $1.24\ \text{\AA}$  for the gas phase molecule.

The dissociative adsorption of  $\text{O}_2$  on the perfect LCM $\{110\}$  is found to be endothermic ( $E_{\text{ads}} = +0.10\ \text{eV}$ ), which suggests that the perfect LCM $\{110\}$  favors molecular  $\text{O}_2$  adsorption rather than dissociative adsorption. The dissociated  $\text{O}^2$  ions adsorb preferentially at top-Ca and Mn sites (Fig. 8, perf-D1). Löwdin population analysis (Table 4) reveal a net charge gain upon  $\text{O}_2$  adsorption, which is responsible for the observed elongated O–O bonds. The  $\text{O}_2$  molecule gained a charge of  $0.26$ ,  $0.44$ ,  $0.33$ , and  $0.53\ \text{e}$  in the M1, M2, M3, and M4 adsorption modes, respectively. In the dissociated state, a combined charge of  $0.40\ \text{e}$  is drawn from the interacting surface Ca and Mn cations.

The stretched O–O bond weakening of molecularly adsorbed structures is confirmed via vibrational frequency analysis, where the stretching frequencies for  $\text{O}_2$  adsorbed in the M1, M2, M3, and M4 adsorption modes are assigned to  $1163$ ,  $691$ ,  $1138$ , and  $710\ \text{cm}^{-1}$ , respectively, all of which are lower than that of the gas phase molecule ( $1558\ \text{cm}^{-1}$ ).

We have also investigated the effect of coverage by employing a larger  $(2\ 1)$  supercell, with a coverage of  $0.25\ \text{ML}$ . We generally found that larger adsorption energies were released at the  $(2\ 1)$  cells compared to the  $(1\ 1)$  cell with a coverage of  $0.50\ \text{ML}$  (parenthesis values in Table 4). For instance, the molecular adsorption energies for  $\text{O}_2$  adsorbed end-on and side-on at top-Mn sites on the  $(2\ 1)$  surface were calculated at  $0.97$  and  $1.22\ \text{eV}$ , respectively, compared to  $0.84$  and  $0.72\ \text{eV}$  at the  $(1\ 1)$  surface. Similarly, larger adsorption energies were calculated for the side-on adsorption at top Ca and bridge Ca–Mn sites at the  $(2\ 1)$  surface compared to the  $(1\ 1)$  surface. The larger  $(2\ 1)$  supercell also favored dissociative adsorption with a highly exothermic energy ( $3.70\ \text{eV}$ ) compared to the endothermic adsorption obtained on the  $(1\ 1)$  surface. The higher exothermic adsorption/dissociation energies calculated in the  $(2\ 1)$  cells compared to the  $(1\ 1)$  cell can be attributed the low  $\text{O}_2$  coverage ( $Y = 0.25\ \text{ML}$ ) in the  $(2\ 1)$  simulation cell, which minimizes repulsive interactions

between the periodic images of the O<sub>2</sub> molecule or its dissociated O ions compared to the high coverage (Y = 0.5 ML) in the (1 1) cell. The strong oxygen binding in the (2 1) simulation cell may lead to a high coverage of dissociated oxygen, effectively passivating the active surface sites. However, seeing that O<sub>2</sub> binding energy at Y = 0.5 ML is smaller than Y = 0.25 ML, under operating conditions, where a monolayer O<sub>2</sub> coverage can be attained, the binding energies may even be weaker due to increased repulsive interactions, thus preventing passivating the active surface sites.

3.4.2 O<sub>2</sub> adsorption on the oxygen-deficient LCM25{110} surface. Similar to the perfect LCM25 surface, we have considered several adsorption geometries and sites at the oxygen-deficient LCM25{110} surface in order to determine the lowest-energy adsorption structures. The optimized adsorption structures are shown in Fig. 9, whereas the calculated adsorption energies and the optimized interatomic bond distances are summarized in Table 4. The adsorption energies for the end-on and side-on configurations (Fig. 9 M1 and M2) of O<sub>2</sub> adsorbed at the top Mn cation sites were calculated at 1.30 eV and 2.14 eV. The interacting O–Mn interatomic distance is calculated at 1.902 Å for def-M1 and 1.829 Å for def-M2, with the O–O bond lengthening from 1.24 Å to 1.41 and 1.44 Å, respectively. Löwdin charge analysis reveals that the O<sub>2</sub> adsorbed in the M1 and M2 modes draws a net charge of 0.44 and 0.47 e, respectively, from the surface Mn cations. The shorter bond distance (1.829 Å) and greater extent of charge transfer (0.47 e)

for the M2 mode is consistent with its stronger calculated adsorption compared to the M1 binding mode.

For the O<sub>2</sub> molecule adsorbed end-on at the top-Ca site, it was observed that the initial configuration is converted to a side-on top-Ca configuration after geometry optimization (Fig. 9, M3) with an exothermic adsorption energy of 1.12 eV. The interacting O–Ca interatomic distance is calculated at 2.256 Å and the O–O bond at 1.35 Å. A net charge of 0.50 e is gained by the O<sub>2</sub> bound to the Ca cation, which resulted in the O–O bond elongation. When O<sub>2</sub> is adsorbed end-on at the vacancy site (def-M4), an adsorption energy of 2.94 eV was released, with the O–O bond significantly elongated to 1.51 Å compared to 1.24 Å in the gas phase. Consistent with the O–O bond elongation, we show from our Löwdin population analysis that the O<sub>2</sub> molecule draws a large charge of 0.76 e upon adsorption at the surface oxygen vacancy.

Similar adsorption characteristics were calculated for O<sub>2</sub> adsorbed side-on at bridge Ca–Mn sites (Fig. 9, M5), with an adsorption energy of 3.28 eV and a net charge of 0.65 e gained by the O<sub>2</sub> molecule. The interacting O–Ca and O–Mn interatomic distances were calculated at 2.280 Å and 1.847 Å, respectively, with the O–O bond elongated to 1.48 Å. Elongation of the O–O bonds was confirmed by the calculated O–O stretching vibrational frequencies: 1284, 615, 979, 433, and 532 cm<sup>-1</sup> for the M1–M5 modes, respectively. The adsorbed molecular oxygen species on the oxygen-deficient LCM25{110} surface can therefore be assigned as superoxo (O<sub>2</sub><sup>-</sup>) and peroxo (O<sub>2</sub><sup>2-</sup>)

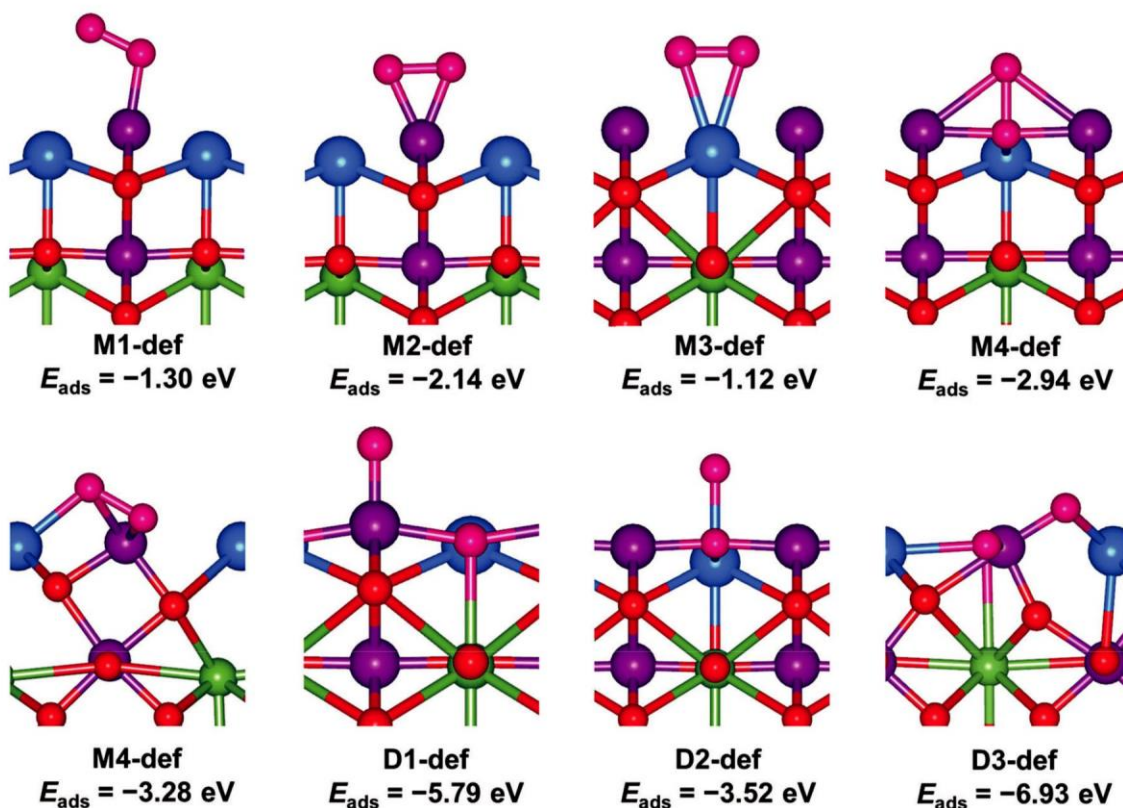


Fig. 9 Side view of the optimized geometry structures of oxygen molecule on defective (1 1) La<sub>0.75</sub>Ca<sub>0.25</sub>MnO<sub>3-x</sub>{110}. Colour code: green = La, blue = Ca, purple = Mn, and red = O.

( $O_2^-$ ) species, based on the calculated stretching frequencies and the O–O bond lengths of (1.35 Å) and (1.41–1.48 Å), which are similar to that of the  $O_2^-$  ion (1.33 Å) and  $O_2^2-$  (1.44).<sup>48,49</sup>

Three dissociative adsorption scenarios were investigated, with the dissociated  $O_2^-$  ions adsorbing at top-Mn and vacancy sites (Fig. 9, D1) or at top-Ca and vacancy sites (Fig. 9, D2) or at vacancy sites bridging Mn and Ca sites (Fig. 9, D3). The adsorption energies of the D1, D2, and D3 modes in Fig. 9 were calculated at 5.79, 3.52, and 6.93 eV, respectively, all of which are more exothermic than the molecular adsorbed structures (M1–M5) and therefore suggest that the oxygen-deficient LCM25{110} surface favours dissociative adsorption over molecular adsorption.

In addition to  $O_2$  adsorption on the (1 1) surface, we have also calculated the adsorption characteristics on a larger (2 1) surface with coverage of 0.25 ML as shown in Fig. 10. Listed in parenthesis in Table 4 are the relevant calculated adsorption energies and the optimized interatomic bond distances. Although similar adsorption geometries were obtained on the (2 1) surface as on the (1 1) surface, the adsorption energies calculated on the (2 1) surface are generally larger than on the (1 1) surface. For  $O_2$  adsorbed side-on at top-Ca cation, end-on at the vacant sites and side-on at bridge-CaMn sites on the (2 1) surface, the adsorption energies were calculated at 1.38, 3.37 and 3.67 eV, respectively, compared to 1.12, 2.94, and 3.28 eV, respectively, on the (1 1) surface. Similarly, the lowest-energy dissociative adsorption modes on

the (2 1) surface release an adsorption energy of 7.50 eV compared to 6.93 eV on the (1 1) surface.

### 3.5 $O_2$ adsorption on the perfect and oxygen-deficient LCM25{100} surfaces

3.5.1  $O_2$  adsorption on perfect LCM25{100} surface. End-on and side-on configurations were examined for the adsorption of molecular  $O_2$  on the LCM25{100} surface (Fig. 11). Summarized in Table 5 are the calculated adsorption energies, the optimized interatomic bond distances, vibrational frequencies and Löwdin charges for adsorbed  $O_2$  at 0.50 ML and 0.25 ML coverages. We have considered a side-on  $O_2$  adsorption at top-Mn site, but found that it converts to the end-on top-Mn configuration after geometry optimization. The calculated adsorption energies of  $O_2$  at the top-Mn site is 0.35 eV at 0.50 ML coverage. The shortest interatomic distance between the interacting oxygen atom and the surface Mn cation (O–Mn) is calculated at 1.958 Å. The calculation was also repeated on a supercell with coverage of 0.25 ML, where adsorption energies of 1.79, 1.43 and 1.37 eV were calculated for  $O_2$  adsorbed end-on at top-Mn site, side-on at the top-Mn site and bridge-Mn–Mn sites, respectively (parenthesis values in Table 5). When the  $O_2$  molecule is adsorbed dissociatively on the two Mn cation sites (D1, Fig. 11), a more negative adsorption energy of 2.04 eV was released.

3.5.2  $O_2$  adsorption on the oxygen-deficient LCM25{100} surface. On the oxygen-deficient LCM25{100}, the adsorption of  $O_2$  end-on at the top-Mn site (Fig. 12, M1) is found to bind

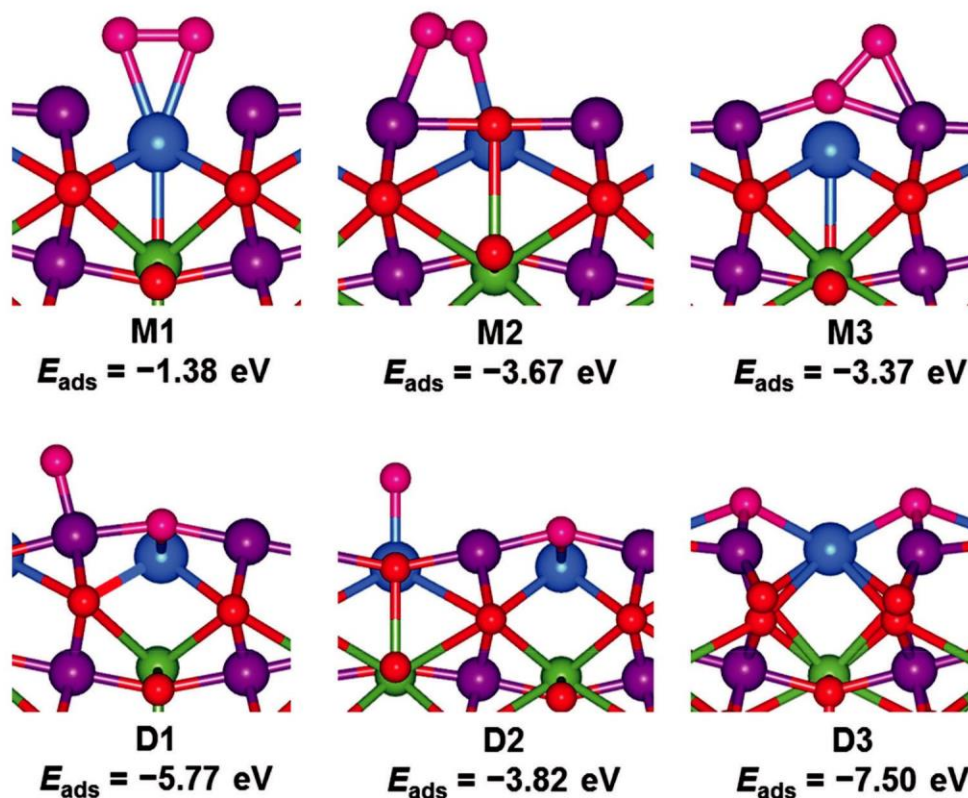


Fig. 10 Side view of the optimized geometry structures of oxygen molecule on defective (2 1)  $La_{0.75}Ca_{0.25}MnO_3 x\{110\}$ . Colour code: green = La, blue = Ca, purple = Mn, and red = O.

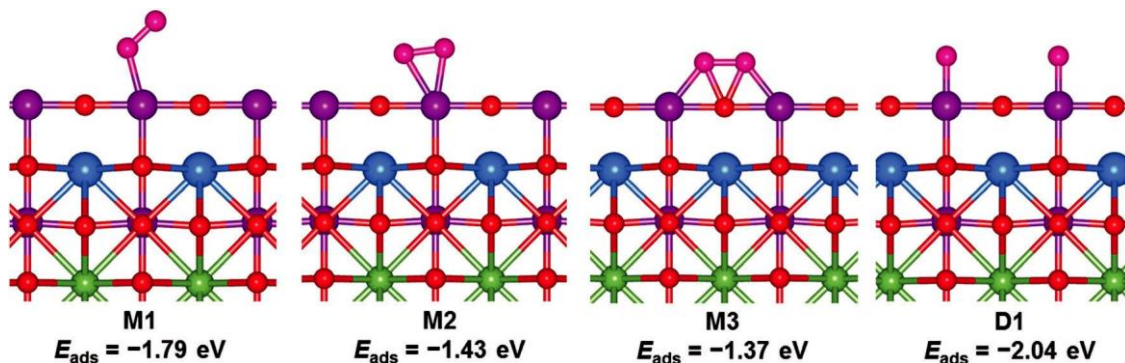


Fig. 11 Side view of the optimized geometry structures of oxygen molecule on perfect (2 1)  $\text{La}_{0.75}\text{Ca}_{0.25}\text{MnO}_3\{100\}$ . Colour code: green = La, blue = Ca, purple = Mn, and red = O.

Table 5 Calculated adsorption energy ( $E_{\text{ads}}$ ), charge ( $q$ ), relevant bond distances ( $d$ ) of molecular ( $\text{O}_2$ ) oxygen on perfect and defective  $\{100\}$ - $(1\ 1)$  surface of LCM25; O–O stretching vibrational frequency ( $\nu$ ) of the adsorbed  $\text{O}_2$ ; and calculated gas phase  $d(\text{O}-\text{O}) = 1.229\ \text{\AA}$  and the  $\nu(\text{O}-\text{O}) = 1558\ \text{cm}^{-1}$ . The  $\{100\}$ - $(2\ 1)$  values are given in parenthesis

	Config	$E_{\text{ads}}$ (eV)	$ q $ (e)	$d(\text{O}-\text{Mn})^{\text{a}}$ ( $\text{\AA}$ )	$d(\text{O}-\text{O})$ ( $\text{\AA}$ )	$\nu(\text{O}-\text{O})$ ( $\text{cm}^{-1}$ )
Perfect	M1	0.35 ( 1.79)	0.03	1.958 (1.927)	1.260 (1.284)	1382
	M2	( 1.43)		(1.952)	(1.381)	
	M3	( 1.37)		(1.924)	(1.390)	
	D1	( 2.04)		(1.662)		
Defective	M1	0.90 ( 2.66)	0.08	1.870 (1.892)	1.282 (1.479)	1280
	M2	0.71 ( 2.97)	0.15	2.088 (1.716)	1.300 (1.393)	812
	M3	2.10 ( 3.87)	0.53	— (1.568)	1.490	496
	D1	3.74 ( 4.81)	0.65	1.580 (1.844)		

<sup>a</sup> The shortest distance between an adsorbed oxygen species and a Mn ion.

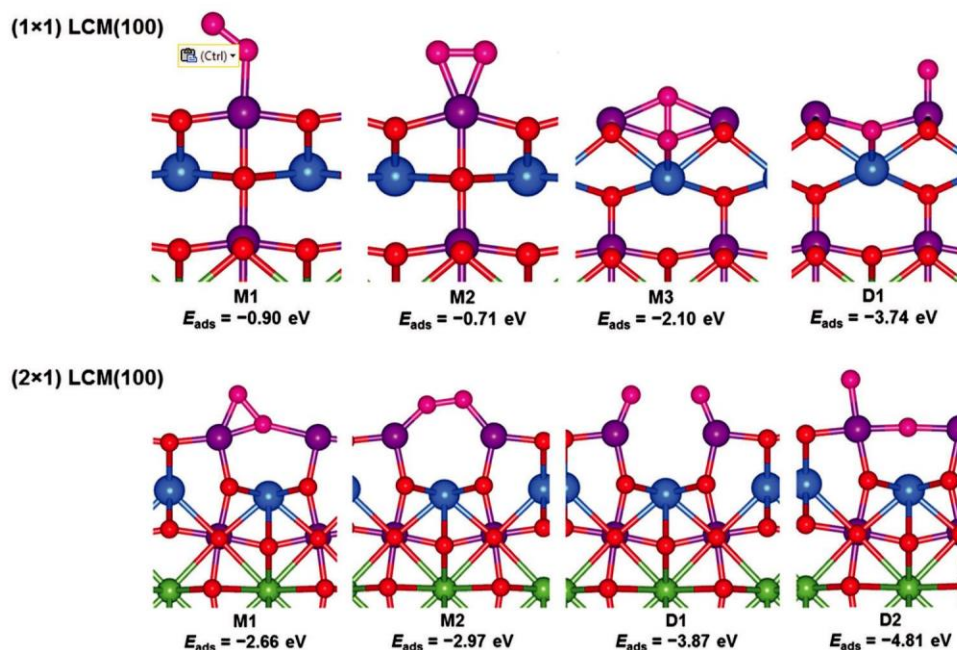


Fig. 12 Side view of the optimized geometry structures of oxygen molecule on defective  $\text{La}_{0.75}\text{Ca}_{0.25}\text{MnO}_3\ x\{100\}$ . Colour code: green = La, blue = Ca, purple = Mn, and red = O.

0.19 eV more strongly than at the side-on top-Mn site (Fig. 12, M2), which is consistent with the shorter Mn–O bond calculated for the top-Mn (1.87  $\text{\AA}$ ) than the side-on top-Mn (2.09  $\text{\AA}$ )

sites (Table 5). However, a larger charge is drawn by the  $\text{O}_2$  adsorbed side-on (0.15 e) than in the end-on configurations (0.08 e), as both oxygen atoms draw charge from the

interacting surface Mn sites in the side-on adsorption configuration compared to the end-on configuration. For O<sub>2</sub> adsorbed end-on at the surface oxygen vacancy sites (Fig. 12, M3), the adsorption energy was calculated at 2.10 eV. A net charge of 0.53 e was gained by the O<sub>2</sub> molecule in the end-on configuration, which results in a calculated elongation of the adsorbed O–O bond to 1.49 Å compared to the gas phase bond length of 1.24 Å. The dissociative (Fig. 12, D1) adsorption of O<sub>2</sub> on the oxygen-deficient LCM25{100} is found to be highly exothermic ( $E_{\text{ads}} = 3.74$  eV), which suggests that the oxygen-deficient LCM25{100} surface favours dissociative O<sub>2</sub> adsorption rather than molecular adsorption. The dissociated O<sub>2</sub> ions, which adsorb preferentially at top-Mn sites and the oxygen vacancy sites (Fig. 12, D1) draw a combined charge of 0.65 e from the surface.

In a larger (2 1) supercell with 0.25 ML coverage, adsorption energies of 2.66 eV and 2.97 eV were calculated for O<sub>2</sub> adsorbed at the oxygen vacancy sites (Fig. 12, M1) and side-on at the bridge-Mn–Mn sites (Fig. 12, M2). When O<sub>2</sub> is placed side-on or end-on at top-Mn site, it was observed that after geometry optimization the initial configuration is dissociated and incorporated into doubly charged surface oxygen vacancies to give D2 (Fig. 12). Similarly, when O<sub>2</sub> is dissociatively adsorbed on the two Mn cation sites (D1, Fig. 12), the process releases an energy of 3.87 eV (Table 5).

To provide atomic-level insight into the effect of Ca-doping on the electronic structures of LaMnO<sub>3</sub> surfaces and their implication for catalytic reactivity, we have plotted the projected density of states (PDOS) for the undoped and Ca-doped LaMnO<sub>3</sub>(110) surface as shown in Fig. 13. It is evident from the PDOS plots that, La ions contribute negligible states at the Fermi level compared to the Mn ions. Since the density of states around the Fermi energy level roughly determines the availability of electrons for a given reaction,<sup>50</sup> it can be inferred that the catalytic activity of the LaMnO<sub>3</sub>(110) surface should be primarily linked to the surface Mn d-states. This helps to explain why the Mn sites are more active than the La sites for O<sub>2</sub> adsorption. It can also be seen from Fig. 13 that Ca doping resulted in a decrease in the Mn-d states around the Fermi level relative to the undoped surface. As the Mn-d states dictate the reactivity of the LaMnO<sub>3</sub>(110) surface, a decrease in their intensity signifies weaker O<sub>2</sub> binding. This helps to explain why the Ca-doped surfaces have weaker O<sub>2</sub> binding energies than the undoped surfaces.

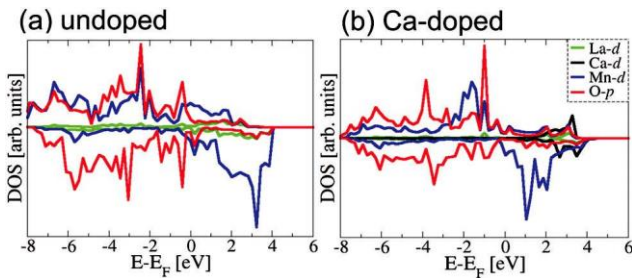


Fig. 13 Projected density of states of (PDOS) for the undoped and 25% Ca-doped LaMnO<sub>3</sub>(110).

3.6 Gibbs free energies  $DG(T,p)$  of the O<sub>2</sub> adsorption/dissociation

In order to estimate the applicability of the calculated adsorption/dissociation energies for typical operating temperatures in SOFCs (500–900 °C), we have calculated the Gibbs free energies  $DG(T)$  of the adsorption/dissociation on these surfaces at typical SOFC operating temperatures and pressures. In the case of adsorption of a gas species on a solid surface, the Gibbs energy of reaction may be written as:

$$DG_{\text{ads}} = G_{\text{surf+adsorbate}} - G_{\text{surf}} - N m_{\text{gas}} \quad (3)$$

where  $N$  is the number of molecules adsorbed in the reaction. By assuming that the presence of the adsorbate does not significantly change the enthalpy nor the entropy of the solid itself, these terms cancel out. The only contributions to the entropy of the surface/adsorbate is then the vibrational entropy of the adsorbates,  $S_{\text{vib}}^{\text{ads}}$ , and the coverage dependent configurational entropy,  $DS_{\text{conf}}^{\text{y}}$ . The vibrational entropy of the adsorbates may be written as:

$$S_{\text{vib}}^{\text{ads}} = \frac{1}{2} N k_B \ln \left( \frac{e^{b e}}{1 - e^{-b e}} \right) \quad (4)$$

where  $b = 1/k_B T$  and  $e^{b e}$  is the total vibrational energy of the adsorbent obtained from normal-mode analysis DFT calculations, and the coverage dependent configurational entropy may be included as:

$$DS_{\text{conf}}^{\text{y}} = k_B \ln \frac{y}{1-y} \quad (5)$$

where  $y$  is the surface coverage. The expression for the Gibbs energy of adsorption then becomes:

$$DG(T,p) = DE^{\text{ads}} + DE_{\text{ZPE}}^{\text{ads}} - \Delta H_{\text{T}}^{\text{gas},0} - T(DS_{\text{conf}}^{\text{y}} + S_{\text{vib}}^{\text{ads}} - S_{\text{gas}}) - N k_B T \ln(p/p^0) \quad (6)$$

with the adsorption energy defined as  $DE^{\text{ads}} = E_{\text{surf+O}_2} - E_{\text{surf}} - N E_{\text{O}_2}$ ,  $p = 0.2$  and  $p^0 = 1$  atm. Correction for errors in the binding energy of O<sub>2</sub> was accounted for by adding 1.36 eV/O<sub>2</sub> obtained from the fitting of experimental formation enthalpy and calculated oxide formation energies.<sup>51</sup> The zero-point vibrational energy (ZPE) is calculated as the difference between the ZPE correction of the adsorbate on the surface and in the gas phase according to eqn (7):

$$DE_{\text{ZPE}}^{\text{ads}} = \frac{1}{2} \sum_{i=1}^{3n} \frac{h \nu_i}{2} - \frac{1}{2} \sum_{i=1}^{3n} \frac{h \nu_i}{2} \quad (7)$$

as where  $h$  is the Planck constant and  $\nu_i$  are the vibrational frequencies. Shown in Fig. 14 is the plot of predicted Gibbs energy of oxygen against temperature for the most stable molecular/dissociative structures of O<sub>2</sub>. It is evident from Fig. 14 that  $DG^{\text{ads}}(T,p)$  is always negative, suggesting that the oxygen reduction reaction is feasible at any of the typical operating temperatures of SOFCs. It is also worth noting that  $DG^{\text{ads}}(T,p)$  values become more negative with increasing temperature, indicating that the oxygen reduction reaction is more feasible

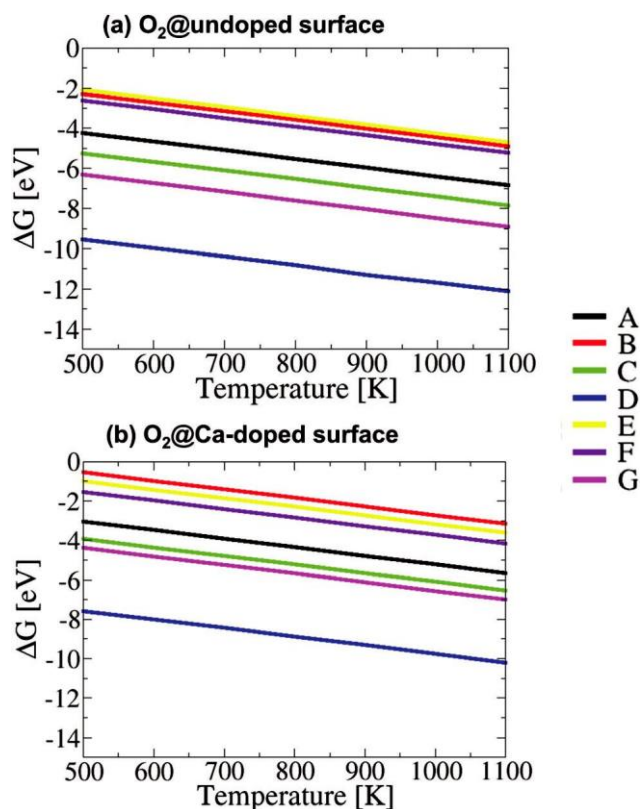


Fig. 14 Gibbs free energies  $\Delta G(T,p)$  of the most stable molecular ( ${}^m\text{O}_2$ ) and dissociative ( ${}^d\text{O}_2$ ) structures  $\text{O}_2$  at the pure (top) and 25% Ca-doped  $\text{LaMnO}_3$  surfaces (down). (Colour code: A =  ${}^m\text{O}_2$ @perfect(110); B =  ${}^d\text{O}_2$ @perfect(110); C =  ${}^m\text{O}_2$ @defective(110); D =  ${}^d\text{O}_2$ @defective(110); E =  ${}^m\text{O}_2$ @perfect(100); F =  ${}^m\text{O}_2$ @defective(100); and G =  ${}^d\text{O}_2$ @defective(100).)

at higher temperatures, which is consistent with the high temperatures employed in operating conditions of SOFCs.

## 4. Conclusions

We have used DFT calculations to investigate the adsorption and activation of  $\text{O}_2$  on the {110} and {100} surfaces of pure  $\text{LaMnO}_3$  and 25% Ca-doped  $\text{LaMnO}_3$ , as materials used in solid oxide fuel cells. We show from our calculations that the adsorption/activation process of the oxygen molecule occurs through the formation of superoxide and peroxide intermediates. The molecular and dissociative adsorption of  $\text{O}_2$  on the pure  $\text{LaMnO}_3$ {110} is shown to be more stable than on the LCM25{110} or LCM25{100} surfaces, as reflected in the stronger calculated adsorption energies. The  $\text{O}_2$  reduction on the LCM25{110} is shown to be energetically more favorable at Mn cation sites than at the Ca cation sites, in agreement with experimental observations, that showed that the B cations are more active than the A cations sites for oxygen reduction in perovskite-type  $\text{ABO}_3$  materials. The adsorption and dissociation process of  $\text{O}_2$  on both pure, doped and oxygen-deficient {100} surfaces are less competitive compared to the {110} surfaces because of a weaker adsorption, implying that the former is catalytically more active for  $\text{O}_2$  reduction. Molecular adsorption was found to be favoured

over dissociative adsorption on the perfect  $\text{LaMnO}_3$  and LCM25{110} surfaces. However, dissociative adsorption is energetically favored over molecular adsorption on the oxygen-deficient {100} and {110} surfaces of pure  $\text{LaMnO}_3$  and LCM25. On the extended surfaces with coverage of 0.25 ML, dissociative adsorption becomes favoured over molecular adsorption on both the perfect and oxygen-deficient surfaces of {100} and {110} LCM25. Lowdin population analysis reveals that the adsorption of oxygen on the pure and Ca-doped  $\text{LaMnO}_3$  surfaces is characterized by significant charge transfer from the interacting surface species which resulted in significant elongation of the O–O bonds of the adsorbed  $\text{O}_2$  molecule. We have compared our calculated  $\text{O}_2$  adsorption energies at the 25% Ca-doped  $\text{LaMnO}_3$  (LCM25) surfaces with other  $\text{ABO}_3$  type cathode materials such as 25% Sr-doped  $\text{LaMnO}_3$ .<sup>24</sup> Generally, the adsorption energies obtained in the present work are more exothermic than those predicted at the 25% Sr-doped  $\text{LaMnO}_3$ , suggesting that Ca-doping can improve the oxygen reduction activity of  $\text{LaMnO}_3$  surfaces more than Sr-doping. Ca-doping is shown to facilitate oxygen-vacancy formation better than Sr-doping on the basis of smaller oxygen-vacancy formation energies calculated at the 25% Ca-doped  $\text{LaMnO}_3$  surfaces than at the 25% Sr-doped  $\text{LaMnO}_3$ .<sup>24</sup> Information on the active sites, adsorption geometries and the nature of the surfaces (perfect or defective) towards  $\text{O}_2$  reduction would be hard to obtain from purely in situ experimental measurements. The molecular-level insights derived from this work shows that first-principles DFT calculations can play a vital role in the rational design of active and efficient  $\text{ABO}_3$  type cathode materials for SOFCs. Future investigations will expand the work presented here to include thermodynamic stability analysis for the  $\text{O}_2$ -LCM25 surface which will enable us to determine the kinetics for oxygen adsorption and dissociation processes as well as predict the optimal range of adsorption energies in  $\text{O}_2$ -LCM25 systems.

## Conflicts of interest

There are no conflicts to declare.

## Acknowledgements

The authors gratefully acknowledge the UK Royal Society and the Leverhulme Trust for a research grant under the Royal Society-Leverhulme Africa Award Scheme. EA, RT and AA also acknowledge the National Council for Tertiary Education, Ghana, for a TALIF research grant. NHdL acknowledges the Royal Society for an Industry Fellowship.

## References

- 1 S. C. Singhal, *Solid State Ionics*, 2000, 135, 305.
- 2 S. C. Singhal, *Solid State Ionics*, 2002, 152–153, 405.
- 3 C. Xia and M. Liu, *Adv. Mater.*, 2002, 14, 521.
- 4 S. C. Singhal and K. Kendall, *High-temperature Solid Oxide Fuel Cells: Fundamentals, Design and Applications*, Elsevier Science, 1st edn, 2003.

- 5 M. K. Debe, *Nature*, 2012, 486, 43–51.
- 6 P. N. Ross, K. Kinoshita, A. J. Scarpellino and P. Stonehart, *J. Electroanal. Chem.*, 1975, 59, 177–189.
- 7 S. B. Adler, *Chem. Rev.*, 2004, 104, 4791–4843.
- 8 J. Fleig, *Advanced Ceramics: Processing and Their Applications*, Elsevier, Amsterdam, 2003, vol. II.
- 9 M. Liu, *J. Electrochem. Soc.*, 1998, 145, 142.
- 10 M. Liu and J. Winnick, *Solid State Ionics*, 1999, 118, 11.
- 11 M. Liu and H. Hu, *J. Electrochem. Soc.*, 1996, 143, L109–L112.
- 12 N. Q. Minh and T. Takahashi, *Science and Technology of Ceramic Fuel Cells*, Elsevier, Amsterdam, 1995.
- 13 B. C. H. Steele, *Solid State Ionics*, 1996, 1223.
- 14 Y. M. Choi, D. S. Mebane, M. C. Lin and M. Liu, *Chem. Mater.*, 2007, 19, 1690.
- 15 Y. Takeda, Y. Sakaki, T. Ichikawa, N. Imanishi, O. Yamamoto, M. Mori, N. Mori and T. Abe, *Solid State Ionics*, 1994, 72, 64.
- 16 B. Delley, *J. Chem. Phys.*, 1991, 94, 7245.
- 17 J. Andzelm and E. Wimmer, *J. Chem. Phys.*, 1992, 96, 1280.
- 18 B. G. Johnson, P. M. W. Gill and J. A. Pople, *J. Chem. Phys.*, 1993, 98, 5612.
- 19 E. Olsson, X. Aparicio-Angle`s and N. H. de Leeuw, *J. Chem. Phys.*, 2016, 145, 199901.
- 20 E. Olsson, X. Aparicio-Angle`s and N. H. de Leeuw, *Phys. Chem. Chem. Phys.*, 2017, 19, 13960–13969.
- 21 E. Olsson, X. Aparicio-Angle`s and N. H. de Leeuw, *J. Chem. Phys.*, 2016, 145, 224704.
- 22 Y. Choi, M. E. Lynch, M. C. Lin and M. Liu, *J. Phys. Chem. C*, 2009, 113, 7290.
- 23 Y. A. Mastrikov, R. Merkle, E. Heifets, E. A. Kotomin and J. Maier, *J. Phys. Chem. C*, 2010, 114, 3017.
- 24 H. T. Chen, P. Raghunath and M. Liu, *Langmuir*, 2011, 27, 6787–6793.
- 25 R. A. Evarestov, E. A. Kotomin, Y. A. Mastrikov, D. Gryaznov, E. Heifets and J. Maier, *Phys. Rev. B: Condens. Matter Mater. Phys.*, 2005, 72, 214411.
- 26 Y. M. Choi, M. C. Lin and M. Liu, *Angew. Chem., Int. Ed.*, 2007, 46, 7214.
- 27 Y. Takeda, R. Kanno, M. Noda, Y. Tomida and O. Yamamoto, *J. Electrochem. Soc.*, 1987, 134, 2656–2661.
- 28 W. Kohn, A. D. Becke and R. G. Parr, *J. Phys. Chem.*, 1996, 100, 12974–12980.
- 29 P. Giannozzi, S. Baroni, N. Bonini, M. Calandra, R. Car, C. Cavazzoni, D. Ceresoli, G. L. Chiarotti and M. Cococcioni, *J. Phys.: Condens. Matter*, 2009, 21, 395502.
- 30 J. P. Perdew, K. Burke and M. Ernzerhof, *Phys. Rev. Lett.*, 1996, 77, 3865.
- 31 H. J. Monkhorst and J. D. Pack, *Phys. Rev. B: Solid State*, 1976, 13, 5188.
- 32 N. N. Kovaleva, J. L. Gavartin, A. L. Shluger, A. V. Boris and A. M. Stoneham, *J. Exp. Theor. Phys.*, 2002, 94, 178.
- 33 P. Ravindran, A. Kjekshus, H. Fjellvag, A. Delin and O. Eriksson, *Phys. Rev. B: Condens. Matter Mater. Phys.*, 2002, 65, 064445.
- 34 A. I. Liechtenstein, V. I. Anisimov and J. Zaanen, *Phys. Rev. B: Condens. Matter Mater. Phys.*, 1995, 52, R5467.
- 35 E. A. Carter, *Science*, 2008, 321, 800–803.
- 36 S. L. Dudarev, G. A. Botton, S. Y. Savrasov, C. J. Humphreys and A. P. Sutton, *Phys. Rev. B: Condens. Matter Mater. Phys.*, 1998, 57, 1505.
- 37 Y.-L. Lee, J. Kleis, J. Rossmeisl and D. Morgan, *Phys. Rev. B: Condens. Matter Mater. Phys.*, 2009, 80, 224101.
- 38 E. Olsson, X. Aparicio-Angle`s and N. H. de Leeuw, *J. Chem. Phys.*, 2016, 145, 014703.
- 39 J. Jilili, F. Cossu and U. Schwingenschlo`gl, *Sci. Rep.*, 2015, 5, 13762.
- 40 F. Zheng and L. R. Pederson, *J. Electrochem. Soc.*, 1999, 146, 2810.
- 41 G. W. Watson, E. T. Kelsey, N. H. de Leeuw, D. J. Harris and S. C. Parker, *J. Chem. Soc., Faraday Trans.*, 1996, 92, 433–438.
- 42 P. W. Tasker, *J. Phys. C: Solid State Phys.*, 1979, 12.
- 43 A. Bielanski and J. Haber, *Oxygen in Catalysis*, Marcel Dekker, New York, 1991.
- 44 G. Herzberg, *Molecular Spectra and Molecular Structure*, vol. 1, 2nd edn, Krieger Publishing Company, Malabar, FL, 1950.
- 45 B. Yoon, H. Ha`kkinen and U. Landman, *J. Phys. Chem. A*, 2003, 107, 4066–4971.
- 46 G. Mattioli, F. Filippone and A. A. Bonapasta, *J. Am. Chem. Soc.*, 2006, 128, 13772–13780.
- 47 J. Mizusaki, N. Mori, H. Takai, Y. Yonemura, H. Minamiue, H. Tagawa, M. Dokiya, H. Inaba, K. Naraya, T. Sasamoto and T. Hashimoto, *Solid State Ionics*, 2000, 129, 163–177.
- 48 P. H. Sit, M. H. Cohen and A. Selloni, *J. Phys. Chem. Lett.*, 2012, 3, 2409–2414.
- 49 U. Aschauer, J. Chen and A. Selloni, *Phys. Chem. Chem. Phys.*, 2010, 12, 12956–12960.
- 50 B. Hammer and J. K. Nørskov, *Adv. Catal.*, 2000, 45, 71–129.
- 51 L. Wang, T. Maxisch and G. Ceder, *Phys. Rev. B: Condens. Matter Mater. Phys.*, 2006, 73, 195107.